ASTRONOMY & ASTROPHYSICS
SUPPLEMENT SERIES

Astron. Astrophys. Suppl. Ser. **122,** 79-93 (1997)

The ATCA/VLA OH 1612 MHz survey

I. Observations of the Galactic Bulge region⋆

M.N. Sevenster[1], J.M. Chapman[2,3], H.J. Habing[1], N.E.B. Killeen[3], and M. Lindqvist[1]

[1] Sterrewacht Leiden, P.O. Box 9513, 2300 RA Leiden, The Netherlands
[2] Anglo Australian Observatory, P.O.Box 296, Epping 2121 NSW, Australia
[3] Australia Telescope National Facility, P.O.Box 76, Epping 2121 NSW, Australia

Received 6 February; accepted 26 June, 1996

Abstract. We present observations of the region between $|\ell| \leq 10^\circ$ and $|b| \leq 3^\circ$ in the OH 1612.231 MHz line, taken in 1993 October and November with the Australia Telescope Compact Array[1]. The region was systematically searched for OH/IR stars and was covered completely with 539 pointing centres separated by $30'$. The size of the dataset calls for a special reduction technique that is fast, reliable and minimizes the output (positions and velocities of possible stars only). Having developed such a reduction method we found 307 OH masing objects, 145 of which are new detections. Out of these, 248 have a standard double-peaked spectral profile, 55 a single-peaked profile and 4 have nonstandard or irregular profiles. In this article we analyse the data statistically and give classifications and identifications with known sources where possible. The astrophysical, kinematical, morphological and dynamical properties of subsets of the data will be addressed in future articles. These observations are part of a larger survey, covering $|\ell| \leq 45^\circ$ and $|b| \leq 3^\circ$, with the Australia Telescope Compact Array and the Very Large Array.

The electronic version of this paper, that includes table and spectra, can be obtainded from http://www.edphys.fr. The table is also available via anonymous ftp (130.79.128.5) or through the World Wide Web (http://cdsweb.u-strasbg.fr/Abstract.html).

Key words: techniques: image processing — surveys — stars: AGB and post-AGB — galaxy: center — radio lines: stars — galaxy i stellar content

Send offprint requests to: M.N. Sevenster

⋆ *Supplement Series.*

[1] The Australia Telescope Compact Array is operated by the Australia Telescope National Facility, CSIRO, as a national facility.

1. Introduction

OH/IR stars are oxygen-rich, cool giants that lose matter at the end of their evolution, in the so-called asymptotic giant branch (AGB) superwind phase (Renzini 1981). The rate at which they lose mass is high ($\sim 10^{-5}\ M_\odot\,\mathrm{yr}^{-1}$), but the expansion velocity is relatively low (10 to 30 $\mathrm{km\,s}^{-1}$). The outflow appears in the form of a circumstellar envelope (CSE) with a chemical composition that varies with radial distance from the star. The composition is determined by, for instance, temperature and ambient UV radiation (see Olofsson 1994). The dust in the outflow absorbs the stellar radiation and reemits in the infrared; the spectrum typically extends from 4 to 40 μm with a peak at 10 to 20 μm. This radiation pumps an OH maser (Elitzur et al. 1976) that forms in a thin shell, on the inside of which H_2O molecules are dissociated into OH and H, on the outside OH into O and H. Various OH lines show maser emission, but we are interested in the strongest, at 1612 MHz, that has an easily recognisable, double-peaked line profile. OH/IR stars represent a wide range of stellar masses; almost all low and intermediate mass (1 to 6 $M_\odot$) stars enter this phase at the end of their life. Little is known about the duration of the AGB superwind phase, but it is thought to depend upon main-sequence mass, and present estimates indicate $\sim 10^{5-6}$ yr (Whitelock & Feast 1993; Vassiliadis & Wood 1993). Since this is only a short time compared to the total lifetime of the star, the objects are relatively rare. In addition to AGB stars, stellar OH 1612 MHz maser emission is also detected from a small number of more massive red supergiant stars (Cohen 1989). We refer to Habing (1996) for an extensive review of the properties of OH/IR stars.

Since their discovery in 1968 (Wilson & Barett), OH/IR stars have become favourite objects for studying very different processes, including, amongst others, stellar evolution and the dynamical behaviour of our Galaxy (Habing 1993). The OH/IR stars (and related objects such as Miras and protoplanetary nebulae (PPNe) (Kwok 1993

and references therein)) are ideal tracers of the galactic potential for a number of reasons. Firstly, the 1612 MHz line (∼18 cm) is not influenced by interstellar extinction, which might otherwise cause a bias in the observed surface density in certain directions because of different optical depths. Secondly, the two narrow peaks of the spectrum yield a very accurate stellar velocity, which is a necessary piece of knowledge in the hunt for the potential. Thirdly, the OH/IR stars have progenitors with a wide range of main-sequence masses and therefore they have a wide range of ages (∼1 to 8 Gyr), while they are all in the same, late, stage of stellar evolution. Such a sample is therefore relatively dynamically relaxed and homogeneous and representative of the stellar content of the Galaxy. Finally, the emission resulting from a maser causes the 1612 MHz line of OH/IR stars to be strong and this enables us to acquire a statistically meaningful sample in a practically meaningful timespan.

In this article we discuss observations (Sect. 2) and reduction (Sect. 3 and Appendix A) of a sample of OH/IR stars (and related objects) in the inner Galaxy (Sect. 4), between $|\ell| \leq 10^\circ$ and $|b| \leq 3^\circ$. We will address this region throughout this article, slightly megalomaniacally, as the "Bulge region". The observations were part of a larger survey with the Australia Telescope Compact Array (ATCA) and the Very Large Array (VLA) of the region between $|\ell| \leq 45^\circ$ and $|b| \leq 3^\circ$, the complete results of which will be presented in due course. A statistical analysis of the sample, partly through comparison with relevant existing data, is presented (Sect. 5). Morphology, astrophysics, kinematics and the dynamical distribution of the sample will be discussed in subsequent articles.

2. Observations

The OH survey observations of the Bulge region were taken with the Australia Telescope Compact Array (ATCA) during 14 days in 1993 October and November. The ATCA consists of six radio telescopes each 22 m in diameter, located along an east-west track, at a geographic latitude of -30°. At a wavelength of 18 cm, the primary beam of each antenna has a full width at half maximum (FWHM) of $29\farcm7$. The array was used in the 6A configuration, which has 15 baselines ranging from 0.34 to 5.94 km. For sources in the Bulge region (at declinations of $\sim -30^\circ$) the longest baseline of 33 kλ (5.94 km) corresponds to an angular resolution of approximately $6''$ in right ascension and $12''$ in declination.

The observations of the Bulge region consisted of a total of 539 pointing centres in the region $|\ell| \leq 10.25^\circ$ and $|b| \leq 3^\circ$. The grid contains 13 rows of constant galactic latitude with an offset of $0\fdg5$ in galactic longitude between adjacent positions within a row. Adjacent rows are offset by $0\fdg5$ in galactic latitude and are shifted by $\pm\ 0.25^\circ$ in galactic longitude. For the $30'$ primary beams of the antennas, the arising "honeycomb" grid pattern provides an almost complete coverage of the survey region (see Fig. 1).

The data were taken in two linear polarizations, using a total bandwidth of 4 MHz and 1024 spectral channels (channel separation 3.9 kHz, correlator frequency resolution 4.69 kHz). The spectral band was centred at 1612 MHz, offset by 0.231 MHz from the rest frequency of the OH groundstate transition at 1612.231 MHz ($^2\Pi_{3/2}\ J = 3/2\ F = 2 \rightarrow 1$). No Doppler tracking (to correct for the Earth's motion around the Sun) was used during the observations. During the observing period of 14 days spread over 5 weeks, the velocity range covered by the observations varied over 12 km s^{-1}, between (-342, $+402$ km s^{-1}) and (-330, $+414$ km s^{-1}). Doppler corrections (radio definition) to the observed frequencies were applied off-line, and the data were Hanning smoothed to give a velocity resolution of 1.46 km s^{-1} (7.8 kHz). After Hanning smoothing, every other spectral channel was discarded, as well as all channels within 9 km s^{-1} of the edges of the spectral bandpasses. In the resulting data the channel separation exactly equals the intrinsic velocity resolution. All velocities are given with respect to the local standard of rest (LSR), assuming a velocity of the Sun of 19.7 km s^{-1} towards right ascension = 18:07:50.3, declination = +30:00:52 (J2000.0).

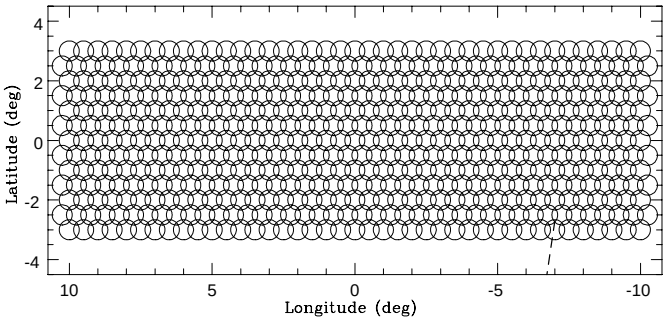

Fig. 1. Grid showing the distribution in galactic coordinates for the pointing centres used in the survey. The diameter of the symbols reflects that of the images ($42'$). This corresponds to a primary-beam attenuation of 0.25 (Sect. 5.1). The dashed line indicates a point at the intersection of 3 fields. That point has the largest possible offset ($19'$) from all surrounding pointing centres in the inner regions of the survey

To optimize the $u - v$ sampling for each pointing centre and to minimize the telescope drive times, the observations were taken using a "mosaic" procedure in the following manner. Each day a single row of the grid was observed, together with calibration sources, for a total time of approximately 12 h. Each pointing centre on a row was observed for 50 s, after which the telescopes were driven to the adjacent position. After completing the scans on the row, the secondary calibrator source $1748 - 253$ (approximately 1.15 Jy at 1612 MHz) was observed for 5 min.

This procedure was then repeated cyclically, so that each pointing centre in the row was observed typically 9 times during the 12 h period, giving a total on-source integration time of typically 7.5 min. For absolute flux density calibrations, the calibrator sources $1934-638$ and/or $0823-500$ were also observed at the start and end of each 12 hour period. The flux density of $1934-638$ at 1612 MHz was taken to be 14.34 Jy (Reynolds 1994). The flux density of $0823-500$ was taken to be 5.82 Jy.

3. Data reduction

In this section we describe all calibration and analysis procedures that we applied to the data. All processing described in this article was done using standard or adapted routines of the MIRIAD (Multichannel Image Reconstruction, Image Analysis and Display) reduction package (Sault et al. 1995). The routines are indicated by their five- or six-letter acronyms in capitals. The reduction was performed largely on a Cray−C98. (See Appendix A for all details on the procedures used).

Radio-frequency interference (RFI) was a major problem of the observations. It is caused by the Russian GLONASS global-positioning satellite system that has a broadband signal ($>$ 0.4 MHz) with sinusoidal ripples across our frequency band and by additional sources with narrowband ($<$ 10 kHz) signals of unknown origin (possibly also GLONASS). RFI is strongest on baselines below 5 $k\lambda$, which are the shortest three baselines of the 6A array. However, considering the decrease of the signal-to-noise ratio (SNR), we decided to discard only the shortest baseline of 2 $k\lambda$. The calibrators were edited to be free from interference using an interactive editing routine (TVFLAG). The bandpass and flux density scale were determined from the sources $1934-638$ and $0823-500$ (MFCAL, GPBOOT). (Two primary calibrators were observed to avoid losing the amplitude calibration in case interference was present all day in the direction of one of them). The time-varying, antenna-based, complex gain solutions were calculated from $1748-1253$ (MFCAL) approximately every hour.

After calibration, we fitted polynomials (UVLIN, Sault 1994) to the spectral baseline of all visibilities in order to subtract wideband interference in all fields automatically. Note that all continuum emission, including point sources, was removed from the visibilities by this fitting. The wideband RFI typically had approximately five maxima and minima across the band which led us to use the high, and odd, order of 11 for the polynomial fit. UVLIN fits the real and the imaginary part of each visibility. It is therefore applicable in low as well as high signal-to-noise situations. For confusing point sources with spectra that are $1^{\rm st}$ order functions of frequency, the high-order fit is very accurate for virtually all offsets of the confusing source, contrary to fits of $1^{\rm st}$-order, that are only applicable when fitting confusing sources close to the phase centre (Sault 1994). For the case of confusing interference (which is neither a point source nor has $1^{\rm st}$-order frequency dependence) the applicability is verified empirically. In general, no other "editing" of the data was done. It is, somewhat surprisingly, more profitable in terms of SNR to keep (slightly) corrupted data and fit them with UVLIN than to rigorously discard corrupted data. This is partly because we have relatively small integration times and partly because neither residual RFI nor the fitting procedure increases the random noise. (There may be systematic errors in the data, but those are easier to recognize). However, particularly bad scans were discarded for some rows of fields with significantly more integration time than others.

To search for sources in the large data set a reduction strategy (MPFND, a routine similar to CLEAN) was developed; this is described in detail in Appendix A. Here, we will only mention its main properties. We do not store the large spectral-line image cubes. Instead, we image the spectral channels one by one, search each for the highest peak, note the peak's position, velocity and flux density and then discard the image. We then compare these highest peaks of all spectral channels of each field to find those that coincide spatially. These are identified as detections of one source at different velocities. They are modelled as point sources and subtracted from the visibilities (UVSUB) of the "motherfield" and from neighbouring fields to remove the confusing sidelobes. This is carried out for all fields and then we repeat the procedure in several iterations until the 3σ level is reached. For further details on the imaging, such as cell sizes and iteration levels, see Appendix A.

After the searching, spectra were extracted, using UVSPEC, from the original visibilities (after calibration, but before polynomial fitting) at all positions where detections had been found. They were checked by eye for their credibility, which was necessary for these data to avoid mistaking any remaining RFI for a source.

4. Results

In Table 1 all OH sources found using the procedures described in Sects. 2, 3 are listed. In total there are 307 sources, 162 of which have been identified with known OH masers. The references for previous OH detections are given in Table 2. Of the 307 sources, we visually identified 248 as having double-peaked (D, see prototype #17) and 55 as having single-peaked (S, see prototype #13) spectra. The remaining four were classified as having irregular (I) spectra, consisting of three or more clearly separated peaks (prototype #123). A reliable IRAS identification is found for 201 sources. For each source the table gives an entry number (Col. 1), the OH$\ell-b$ name (Col. 2), a type (D, S, I) identifier (Col. 3), position in J2000 coordinates (Cols. 4, 5), a measure of the error in the positions (Col. 6), the distance from the source to the pointing centre (Col. 7), the peak, stellar and outflow velocities

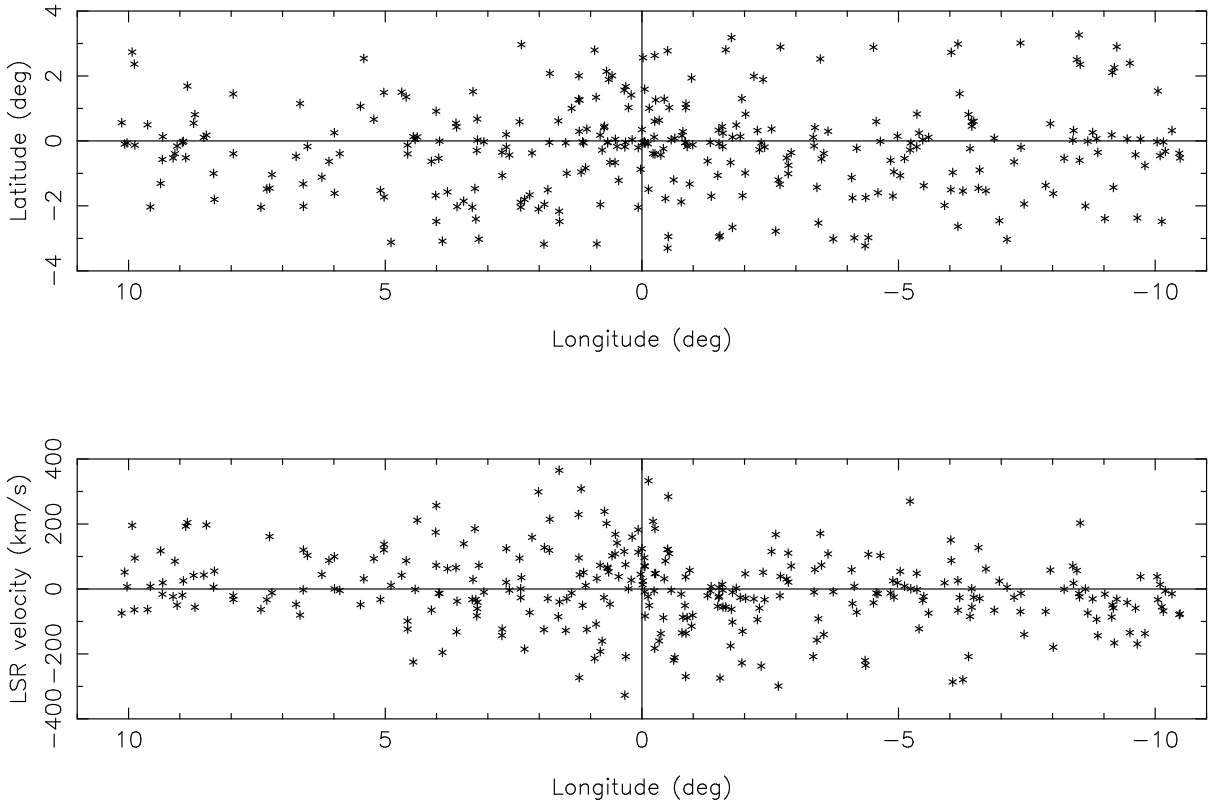

Fig. 2. The longitude-latitude diagram and the longitude-velocity diagram for all objects of Table 1. Features in these diagrams will be discussed in a future article

(Cols. 8 to 11), the peak flux densities (Cols. 12, 13), the noise in the field where the source was detected (Col. 14, velocity resolution 1.46 km s^{-1}), the number of the reference to previous observations if applicable (Col. 15), the name of the nearest IRAS point source (Col. 16) and the distance to this nearest IRAS point source expressed as a fraction of the corresponding IRAS error ellipse (Col. 17). A detailed discussion of the data set is given in Sect. 5.

In Fig. 3 the longitude-latitude diagram and longitude-velocity diagram are shown for all 307 sources. The spectra for all the sources in Table 1 are shown in Fig. A2. They are displayed with 50 $\mathrm{km\,s^{-1}}$ on either side of the stellar velocity. The channel width used in the spectra is 1.46 $\mathrm{km\,s^{-1}}$ which is equal to the velocity resolution. Along the upper border of each spectrum the entry number of the source in Table 1 is given, along with the usual OH$\ell - b$ name, its identification as double-peaked, single-peaked or irregular source and the number of the reference in the case of previously known sources.

To give a fair view of the data quality, spectra were extracted with the MIRIAD routine UVSPEC from the original visibilities, without any removal of interference. Spectral baselines were then fitted with polynomials of order up to three. This enables us to determine accurate flux densities although interference signals can clearly be seen in the spectra of some sources. Also, sidelobes from neighbouring stars are present in some spectra (positive as well as negative). If confusion is possible, the real peaks are indicated by an asterisk (e.g. spectrum #109).

Table 1 and Fig. A2 can be obtained with the electronic version of the whole paper (http://www.edphys.fr). The table is also available via anonymous ftp (ftp 130.79.128.5) or through the World Wide Web (http://cdsweb.u-strasbg.fr/Abstract.html).

5. Data analysis

In this section we analyse the global completeness of the survey and discuss the statistical accuracy of parameters given in Table 1. We will, unless stated otherwise, assume that errors obey the laws of normal distributions.

5.1. Survey completeness

5.1.1. Noise levels

Figure 3 shows the empirically determined rms noise level for each of the fields in the Bulge region. For each field, the diameter of the circle is proportional to the rms noise level in the image planes (averaged over all spectral channels in an image cube after the removal of all detected point sources and subtraction of the background continuum level (Sect. 3)).

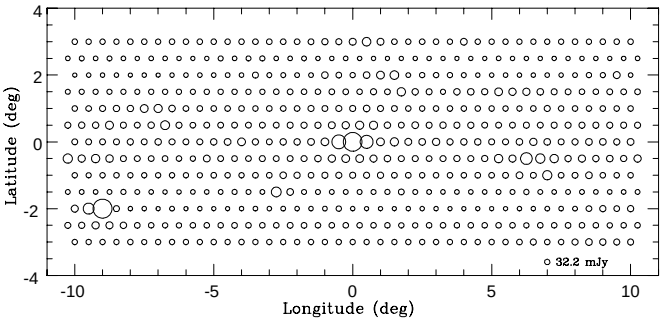

Fig. 3. The empirical noise for the different pointing centres. The diameters of the circles are proportional to the noise levels. The size of the circle corresonding to the average noise level of 32.2 mJy is shown in the lower right corner

The empirical noise is lower than the noise expected theoretically (from e.g. system temperature and number of visibilities) by about 10% as a result of the inevitable interpolation in the calculation of velocities from the observed frequency channels.

The $11^{\rm th}$-order polynomial fit (see Sect. 3) causes a decrease in the rms noise levels of ∼2%. The empirical rms noise level, averaged over all fields, is 32.2 mJy while 90% of fields have noise levels below 40 mJy. Higher noise levels are evident in some fields due to higher system temperatures arising from RFI, or, for fields close to the galactic Centre (GC), from the proximity of the strong radio emission from Sgr A. The highest empirical noise level, 106 mJy, occurs in the field covering the GC.

5.1.2. Detection levels

Figure 4a shows the primary beam response (PBR) of the ATCA antennae at 18 cm as a function of radial offset from the pointing centres (Wieringa & Kesteven 1992). The FWHM of the response function is at $29\farcm7$. The offset labelled "max" corresponds to the offset within which the flux density of a source is always greater at the true source position than at a position measured from a "ghost" image (see Appendix A).

For inner fields, the largest possible offset for a source is $19'$, which coincides with the full width at 0.32 of the global maximum. For the fields in the outer corners of the survey (4 out of 539), the largest possible offset is determined entirely by the image size set in the imaging routines, which is $42'\times 42'$ (Appendix A). The maximum offset in images is therefore $29\farcm6$, which corresponds to a PBR of 0.023. As can readily be seen from Fig. 4b, no sources have been detected at such low PBR levels; the largest offset detected is $21'$ (PBR 0.25). This is not surprising; not only is the PBR very low but also the total area of the survey covered by offsets larger than $21'$ is only 2%.

Because of primary beam attenuation, the detection level for OH maser emission in the survey is not uniform across each field, but increases with the radial offset of a source position from the field centre. For the detection of stellar masers, we set an absolute detection level at 120 mJy, corresponding to approximately three times the noise level in "poor" fields. After correcting the OH flux densities for primary beam attenuation, we would therefore expect to detect sources with peak flux densities above 0.12 Jy near the pointing centres, and above $(0.32)^{-1}\times$ 120 mJy = 375 mJy at offsets of $19'$ from the field centres.

In Figs. 4b to 4f we investigate the global completeness of the survey. Figure 4b shows the PBR of each source against the measured peak flux density, corrected for primary beam attenuation. The PBR for each source is directly related to the source offset and is calculated using the curve shown in Fig. 4a. The solid line connects stars with the lowest detected OH flux densities, determined in PBR bins of width 0.1. From this diagram it is evident that nearly all detected sources have PBR values above 0.3, corresponding to offsets within $19'$ of the field centres. Of the total area of the surveyed region, 95% is within this offset. In addition, a few sources were detected at larger offsets in the fields at the boundary of the Bulge region surveyed. The dashed line in Fig. 4b indicates the expected relation between PBR and flux density cut off for an absolute detection limit of 160 mJy, which is the best fit. In the final sample, the limiting flux density corrected for primary beam attenuation is found to be 160 mJy or $\sim 4\sigma$. The noise levels do not vary (strongly) with offset but the primary beam attenuation does. This means that the detection limit is changed for offset smaller than $10'$, where the PBR is more than 0.75. In those regions one could in principle expect to find sources that have a flux density of ∼120 mJy after correction. However, in the visual inspection the spectra of those sources, that have a SNR of less than 4, where not found to be acceptable (Sect. A5). In Fig. 4f the SNR for all objects with SNR < 40 from Table 1 is plotted against their offset. Indeed, the limiting SNR is constant at 4 out to $10'$ in offset. Only for larger offsets is the SNR slowly rising with offset because there the limiting factor is not the 4σ detection level in corrected flux density but the 120 mJy detection level in uncorrected flux density. At $20'$ the PBR is 0.28 and we expect a cut off at 120 mJy/0.28 = 430 mJy or at a SNR of 10 to 11. In Fig. 4f this is indeed found to be the limiting SNR.

In Fig. 4c we plot the cumulative flux density distributions for the detected sources with PBR > 0.8 (solid line) and, for comparison, with PBR < 0.6 (dashed line). Because the minimum detected flux density is almost independent of PBR for high PBR (Fig. 4b), we estimate that the survey was essentially complete for PBR > 0.8, given the survey detection limit. The solid line shown in Fig. 4c therefore provides a reasonable approximation to the intrinsic cumulative flux density distribution for the OH/IR stars in the present sample.

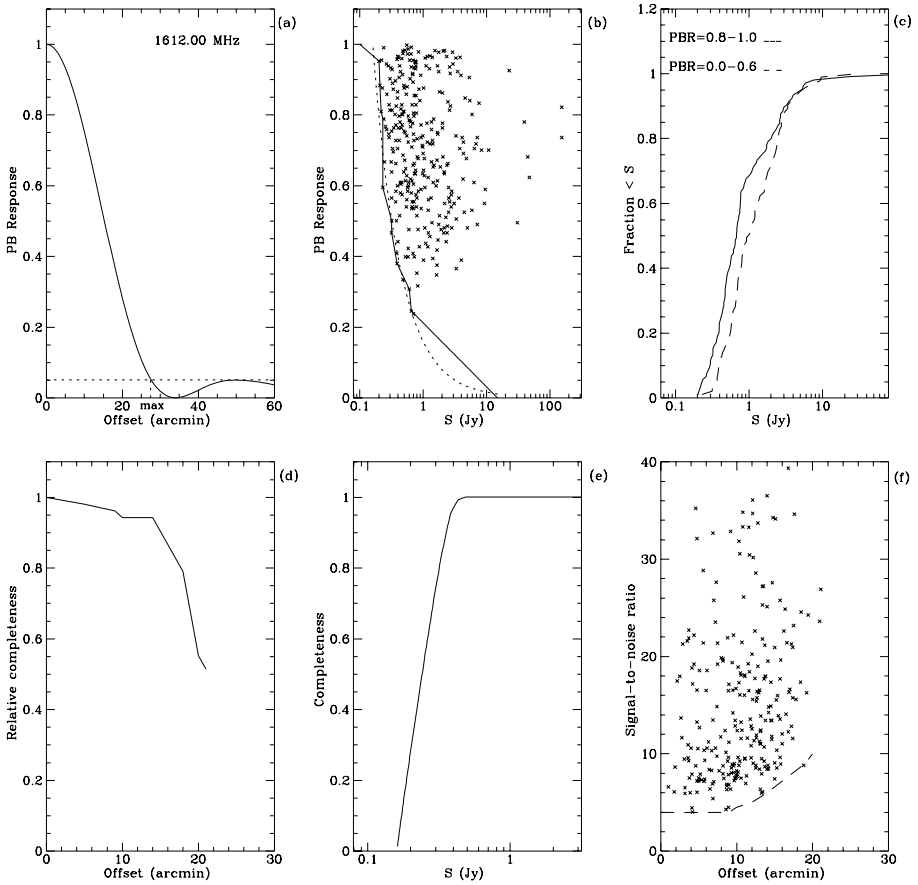

Fig. 4. Representation of the completeness of the data. **a)** The primary beam response (PBR) of the ATCA antennae at 18 cm, as a function of radial offset from the pointing centre, taken from Wieringa & Kesteven (1992). The offset labelled "max" indicates the offset to which the measured flux density of a genuine source is always higher than the flux density measured for a "ghost" image of that source. **b)** The PBR calculated for the detected sources plotted against the peak OH flux densities, corrected for primary beam attenuation. The solid line indicates the lowest flux densities detected for PBR bins of width 0.1. The dashed line indicates the expected inner boundary calculated from the PBR curve in **a)** for a limiting flux density of 160 mJy (best fit). **c)** The cumulative flux density distribution for stars with PBR values > 0.8 (solid line) and < 0.6 (dashed line). The solid line is taken to be the intrinsic OH flux density distribution for the sources in the survey. **d)** The completeness, relative to the pointing centres, of the survey as a function of position offsets from the field centres. An offset of $15'$ corresponds to half the distance between nearest fields in a row of constant latitude (Fig. 1); $21'$ is the largest observed offset in the survey. **e)** The completeness of the sample as a function of flux density. The offset out to which a source with certain flux density can be observed is determined from the dotted line in **b)**. Then we integrate the completeness given in **d)** from that offset to zero, normalizing with surface. **f)** The SNR for all sources with SNR lower than 40, plotted against their radial offset from the pointing centre. The dashed line shows the lower limit for the SNR at a certain offset

In Fig. 4d we plot the relative completeness of the survey as a function of source offset from the pointing centres. For this diagram we have combined the information given in Figs. 4a to 4c, and have assumed that the solid line shown in Fig. 4c is the intrinsic flux density distribution for the sources in the surveyed region. A sudden decrease in completeness takes place at $\sim 14'$. The completeness is a function of the value of the PBR at a certain offset and of the total area where the PBR has that value. The fields start overlapping at offsets of $15'$ because the smallest distance between pointing centres is $30'$ (on the same latitude row; see Fig. 1). Therefore the surface filled by all points with an offset larger than $15'$ is no longer a complete annulus. Whereas for offsets smaller than $15'$ the increasing area and decreasing PBR seem to balance each other into almost constant completeness, above this offset both PBR and area decrease, and so does the completeness.

In Fig. 4e we plot the completeness of the survey as a function of flux density, combining Figs. 4b and 4d. For the derivation of the curve in Fig. 4e, we have to integrate the completeness given in Fig. 4d from the largest offset possible for a source with a certain flux density inward to offset $0'$, normalizing with area (see above). For sources of 375 mJy that can, as discussed, be found at

all offsets $< 19'$, or in other words in 95% of the survey area, the completeness is 0.95, as found from Fig. 4e. This is a coincidence; for instance, for sources of 200 mJy (offset $< 13'$, area 58%) the survey has a completeness of 0.2. As expected, the curve levels out for flux densities above 120 mJy / 0.25 = 480 mJy (offset $21'$).

So far, this discussion has been about the global completeness of the survey. As discussed in Sect. 5.1.1, the noise levels vary from field to field and therefore the detection level will also vary. For the fields close to the GC the degree of completeness is likely to be lower than elsewhere due to the higher noise levels in the images (Fig. 3). For example, in the central GC field the empirical noise is 106 mJy. If we assume that the detection limit is 3σ (although set to 120 mJy), we expect the survey to be complete in this field for sources brighter than 3×106 mJy/ $0.32 = 0.99$ Jy and to have an absolute flux density cut off at 318 mJy. Figure 4c shows then that 20 to 70% of the intrinsic flux density distribution is unobservable in this field[2]. The equivalent of Fig. 4e for individual fields can be obtained by shifting the curve in the horizontal direction, shifting to the right for increasing noise levels. The slope of the curve does not change since we assume the noise levels are constant over one field or, in other words, we assume Fig. 4d does not change from field to field.

5.2. Positions

The positions of sources were determined by fitting a parabola (MAXFIT) to the 3×3 cells centred on the pixel with the highest value found in a plane (see Appendix A). The difference between this fitted position and the genuine position of a source depends upon the size of the image cells relative to the size of the synthesized beam and upon the shift of the centre of the central cell with respect to the source position. Naturally, there is no guarantee that the imaging procedure will put stars exactly in the centre of an image cell. In Fig. 5 we plot the error in the fitted position as a function of cell size for various SNRs and shifts of the centre cell with respect to the source position. The errors are found using simulated data by fitting parabolae to Gaussian-shaped peaks with added random noise. The maximum shift is necessarily half a cell, since we ensure in the searching method (Appendix A) that the highest peak value is at the cell that is at the centre of the 3×3 cells. When the cells are so small that all 9 cells to be fitted sample the tip of the Gaussian, we are essentially fitting a parabola to a flat line. Therefore, in all panels we see that the errors increase for cell sizes below 0.2 HWHM. When, on the other hand, the cell sizes are so large that all cells except for the central one have a value of essentially zero, we are essentially trying to fit a parabola to a delta function and again the errors increase for cell sizes above 3 HWHM.

For the cell sizes ($\sim$1 HWHM, both in right ascension and declination) and SNRs (4 to 4000) used in the imaging, the positional errors are typically 0.1 cell size. With cell sizes of $2\farcs5 \times 5''$, this translates to a positional error of $\sqrt{(0.25^2 + 0.5^2)} = 0\farcs56$, with the largest contribution in declination.

From calibration errors we expect a positional error of less than $0\farcs2$ because of fluctuations in the phase gain solutions of about $10\fdg0$.

The positions given in Table 1 are the positions of the star measured in the channel with the strongest peak. This gives the most accurate position of the source because the SNR is larger than in intermediate channels (see Fig. 5). The entry Δ (Table 1, Col. 6) is defined as

$$\Delta = 1/M \cdot \sum_{N=2}^{M} \Big((\cos\delta_N * \alpha_N - \cos\delta_{N-1} * \alpha_{N-1})^2 + (\delta_N - \delta_{N-1})^2 \Big)^{\frac{1}{2}} .$$

It gives an indication of the mean scatter in the position of the star measured in all the channels where it was detected. It should be carefully interpreted as an upper limit to the individual positional errors of the sources, because it depends upon various quantities, such as flux, angular size (for average source properties the angular size in intermediate channels can be of the order of $0\farcs1$) and pass of detection. The typical value for Δ in Table 1 is $0\farcs5$.

In summary, the positional error is at worst a bit more than $1''$; for most sources, however, the positional error is $\sim 0\farcs5$, with the largest contribution in the declination.

5.3. Flux densities

The OH peak flux densities given in Table 1 were determined directly from the spectra and corrected for primary beam attenuation. The absolute calibration of the flux density scale is accurate to a few per cent while time-dependent flux density variations were calibrated to give flux densities accurate to $< 10\%$. The ATCA antennae have rms pointing errors of approximately $10''$ giving an additional error in the measured flux densities of maximally 3%, varying with offset.

The measured OH peak flux densities are dependent on the velocity resolution of the measurements. The spectra have a velocity resolution of 1.46 $\mathrm{km\,s^{-1}}$, considerably broader than the natural linewidth of the OH emission features in OH/IR stars. This leads to a significant decrease in the measured OH

[2] However, we note that the luminosity function and hence flux density distribution of OH/IR stars may be different for stars close to the galactic Centre, with slightly higher OH luminosities than elsewhere in the Galaxy (Blommaert et al. 1992). If this is the case, then we would expect to have detected a higher fraction of stars in the central field, but this is hard to quantify.

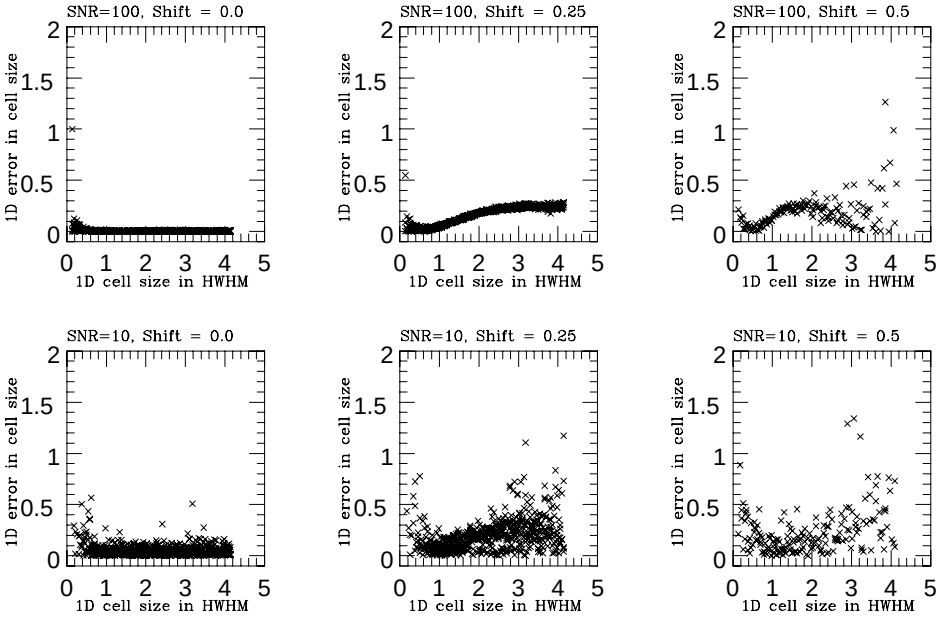

Fig. 5. The error in the fit as a function of cell size, as found from simulations. For each of the 100 steps in cell size 100 simulations of the fitting procedure were done on a perfectly Gaussian-shaped peak with added random noise. The upper panels show the error in the fitted position for a SNR of 100, the lower panels for SNR of 10. From left to right the shift of the gridded pixel positions with respect to the true source position is increasing from 0.0 to 0.5. The cell sizes are given in units of one HWHM of the synthesized beam; the errors in cell size. A horizontal line in any of the panels therefore means that the positional error grows linearly with absolute cell size

peak flux densities compared to data taken with higher velocity resolution. This effect is strongest for the steepest spectral profiles. For 12 of the sources in the Bulge region, we have compared the ATCA spectra with single-dish OH 1612 MHz spectra obtained by Chapman et al. in the same epoch as our data, using the Parkes 64 m radio telescope with a velocity resolution of 0.36 $\mathrm{km\,s^{-1}}$ (J.M. Chapman, private communication). The peak flux densities for the 12 sources are a factor of 1.3 to 1.8 smaller in our data than in the single-dish spectra, but the fluxes are comparable when the single-dish spectra are smoothed to the same velocity resolution. Apart from this undersampling error that depends only on the intrinsic profile, the flux densities inevitably decrease when interpolating linearly to find the velocities from the observed frequency channels. This effect causes an underestimate in the flux density of as much as 25% at worst, but typically of 5%. (The rms noise level in the spectra is decreased by about 10% by the same effect (Sect. 5.1.1)).

We conclude that, for the velocity resolution of 1.46 $\mathrm{km\,s^{-1}}$, the OH peak flux densities are systematically too low by ∼5%, with an additional random error of typically 5%.

5.4. Velocities

The velocity resolution (FWHM) of the data, resulting from Hanning smoothing 1024 channels in a 4 MHz bandwidth is 1.46 $\mathrm{km\,s^{-1}}$, which equals the channel separation after we discard every second channel. Spectral gridding and interpolation causes errors of typically half a FWHM in the peak velocity determination, from arguments similar to those used in Sect. 5.2. When the flux density difference between neighbouring channels for a detected source are of the order of the amplitude of the noise then the detected peak can easily shift one channel if the noise adds to the flux density in the channel with the intrinsically second strongest signal. This is enhanced by the fact that neighbouring channels are correlated by about 16% after the Hanning smoothing. Therefore the typical error in all velocities given in Table 1 (Cols. 8 to 11) is 1 $\mathrm{km\,s^{-1}}$.

Because the intrinsic shape of the (double-peaked) spectra is such that peaks are, in general, steeper at the outer edge than at the inner, smoothing will cause the outflow velocity to decrease slightly, rather than changing it in a random way.

A few effects relating to velocity coverage need to be considered. Firstly, owing to the changing Doppler shift the velocity band shifted by about 12 $\mathrm{km\,s^{-1}}$ over the observing period of two months. Secondly, when fitting the continuum with UVLIN the polynomial can "roam freely" and increase the noise at the outer 5% of the band. Thirdly, there may be double-peaked sources that have only one peak in the observed velocity band; these appear to be single-peaked sources and are therefore less likely to be detected (Sect. A4).

These three factors limit the homogeneously covered velocity range to (-280, $+300$ km s^{-1}). Ten sources where detected with one or more peaks outside this range, six at negative and four at positive extreme velocities. Four are identified as single-peaked sources, indicating that the second peak may be outside the velocity range searched. In fact, one, source #179, is a famous double-peaked source, Baud's star (Baud et al. 1975), which has a second peak at -356 km s^{-1}. These numbers suggest that there is no need for concern about missing sources as a result of velocity-dependent effects. The fact that the band extends to more extreme positive velocities than negative velocities does not introduce a large bias either, as already implied by the numbers of extreme velocity sources mentioned above. The negative extreme of the velocity range covered is at -320 km s^{-1}; only two sources have velocities higher than $+320$ km s^{-1}.

Figure 6a shows the distribution of the stellar velocities for the detected sources. Figure 6b shows the distribution of expansion velocities for the double-peaked sources. Nearly all double-peaked sources have expansion velocities between 4 and 30 km s^{-1} with a peak in the distribution at velocities near 14 km s^{-1}. Expansion velocity histograms for other observations invariably show very similar distributions (Eder et al. 1988; Habing 1993). However, there are two sources (#008, #200) with extremely high outflow velocities, 65.7 km s^{-1} and 78.8 km s^{-1} respectively. Although OH/IR sources with outflow velocities up to 90 km s^{-1} are known (te Lintel Hekkert et al. 1992), they are very rare and mostly the outflow velocities are not derived from the OH 1612 MHz spectrum but from CO or other OH maser lines. These sources are mostly found to be PPNe. For the two extreme-outflow-velocity sources in our sample no counterparts have been found in the literature. We will not speculate upon their nature in this article.

In summary, the typical error in stated peak velocities in Table 1 is 1.0 km s^{-1}. The errors are independent of velocity. (For S (and possibly I) sources it should be realised that the stellar velocities deviate from the real stellar velocities by one average outflow velocity, of the order 14 km s^{-1}).

5.5. IRAS identifications

For each of the sources in Table 1, Col. 16 gives the nearest IRAS point source identification, obtained using version 2 of the IRAS Point Source Catalog (PSC). The parameter N in Col. 7 is defined as the ratio of the distance to the nearest IRAS point source to the size of the IRAS error ellipse *in the direction towards the source*. In general the IRAS error ellipses are highly elongated and much larger than the errors in the OH positions; they are of the order of $30'' \times 7''$. They define the 2σ errors in the IRAS positions (i.e. 95% likelihood). The ratio N is, therefore, contrary to the absolute distance from the infrared to the OH position, directly related to the probability of an association between the OH and infrared sources. For example, for $N = 1$, the OH position lies on the 2σ IRAS error ellipse, and the likelihood of an association between the radio and infrared sources is 5%.

In the Bulge region, the IRAS observations were highly confused and many infrared sources could not be identified as point sources. For this reason we expect the number of associations between the OH and infrared sources to be small. For all 307 sources the average distance to the nearest IRAS PSC position is $44''$; 201 (65%) have an IRAS identification within the error ellipse ($N \leq 1$). Of those 201, we plotted the ones with reliable IRAS-colour determination (see IRAS Explanatory Supplements) in Fig. 7, the two-colour diagram as described by van der Veen & Habing (1988).

5.6. OH identifications

The OH identifications given in Table 1 (Col. 15), with references in Table 2, were obtained using the Simbad (Centre de Données de Strasbourg) database, which was searched for previous OH 1612 MHz maser detections within $1'$ for each source. Most detections of stellar OH 1612 MHz maser emission that were made before 1989 are comprised in the catalogue by te Lintel Hekkert et al. (1989, (02)). For sources in that catalogue we do not give the original references. It would not be realistic to claim that all sources without identification within $1'$ are new detections, since some of the known OH masers have positions taken directly from the (assumed) associated IRAS point source and these can be wrong. This is the case for, amongst others, spectrum #258. No reference is given in Col. 15, but the source has been detected by te Lintel Hekkert et al. (1991, PTL) at the location of IRAS $17565-2035$. However, we find IRAS $17560-2027$ to be closest to #258. The new position differs from the previous by $11'$. On the other hand, for some of the sources detected by PTL, better positions were already known and for those the reference to the detection of the improved position is given (e.g. #101, #270, van Langevelde et al. 1992, 08). It is obviously hard to give proper credit to references to previous detections of OH maser sources. However, the new positions are so much more accurate that we feel justified in counting those few sources as new. The number of sources in Table 1 without a previous OH detection in Col. 15 is 145 (47%).

The ATCA survey of the Bulge region overlaps considerably with the earlier single-dish detection experiment by PTL. The PTL survey used the Parkes 64 m telescope, with a resolution of $12\farcm6$, to search for OH 1612 MHz emission from IRAS-selected sources. In the Bulge region, PTL detected OH 1612 MHz maser emission from 145 sources, of which we detected 78 sources in the ATCA survey. The sensitivity of their survey is comparable to that of the ATCA survey. However, we will have observed

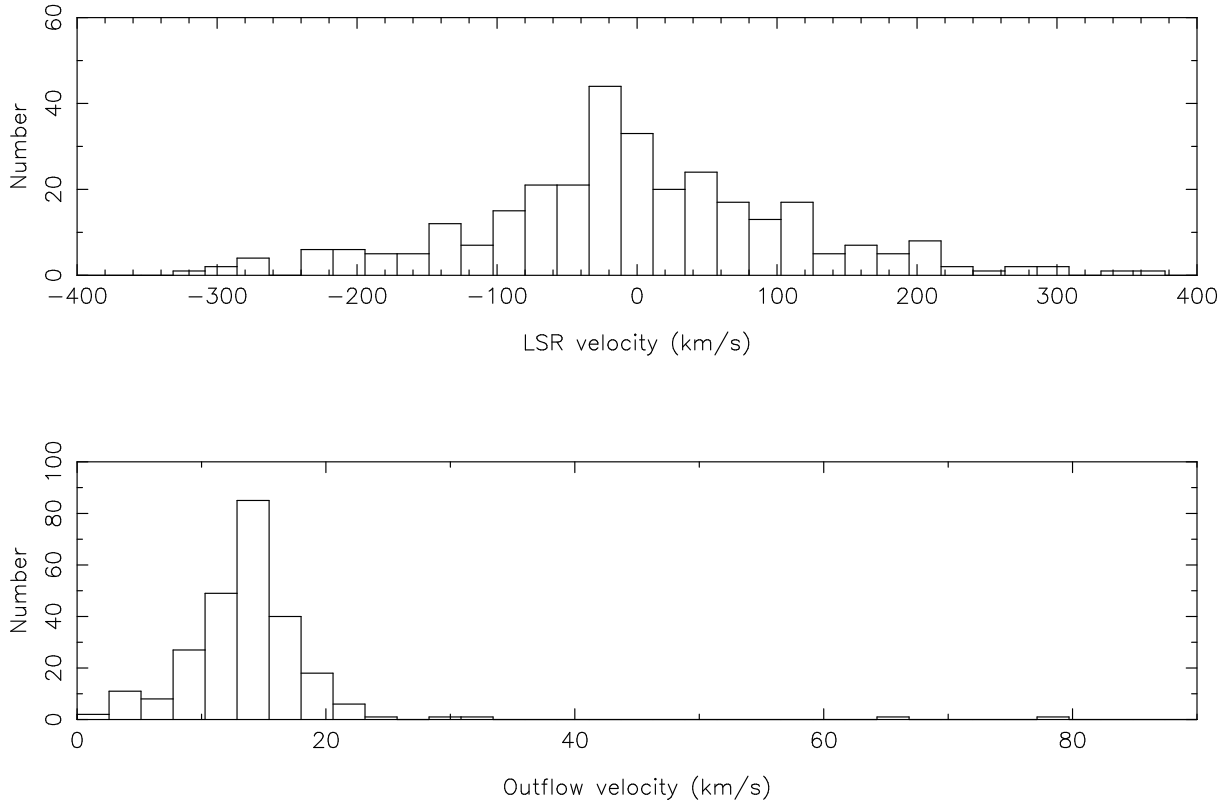

Fig. 6. a) LSR stellar velocity distribution for all sources in Table 1. Note that for the single-peaked sources the stellar velocities are taken to be at the velocity of the emission peak. For these stars the true stellar velocities may differ by $\sim$14 $\mathrm{km\,s^{-1}}$. **b)** The outflow velocity distribution for all 245 double-peaked objects in Table 1. The average of all outflow velocities is 14 $\mathrm{km\,s^{-1}}$. Features in these diagrams will be discussed in future articles

most of the PTL sources with considerable primary beam attenuation. Besides this, OH/IR stars are variable with typical periods of one or two years. In the 8 years between the two surveys, a set of stars with similar flux densities in the PTL survey will have spread over a wide range in flux density. Taking these two effects into account, we calculate the fraction of the PTL sources we would expect to redetect to be around 60%, which is consistent with the actual number of redetections. (Of course the reverse is equally true; sources we detect were not found in the PTL survey).

Lindqvist et al. (1992) made a very deep survey for OH/IR stars towards the central degree of the Galaxy, with an rms noise level of 20 mJy, and found 134 double-peaked objects. Our data include 19 detections in common.

Some I objects or nonstandard D objects are known to be objects in transition from the AGB to the planetary-nebula phase, e.g. #134 (extreme peak-flux ratio, see Zijlstra et al. 1989) or supergiants, e.g. #299 (irregular peaks, VX Sgr, see Chapman & Cohen 1986).

6. Summary

We have given the results of a survey of the region $|\ell| \leq 10^\circ$ and $|b| \leq 3^\circ$ in the OH 1612.231 MHz maser line. The survey is complete for sources brighter than 500 mJy and 80% complete for sources brighter than 300 mJy. The absolute flux density limit is 160 mJy. We have found 307 compact OH-maser sources, 145 of which are new detections. The sources are mainly OH/IR stars, with a few related sources, like PPNe and supergiants. The sources have positions accurate to $0\farcs5$, velocities accurate to 1 $\mathrm{km\,s^{-1}}$ and flux densities accurate to 5%. For 201 sources, an associated IRAS point source is found. A special CLEANing method was developed to search a very large data set for spectral-line point sources.

Acknowledgements. The authors thank ATNF staff for valuable discussions about observations and reduction, especially Ron Ekers, Wim Brouw and Jim Caswell. MS thanks the NFRA for financial support, the ATNF for infinite hospitality, Richard Arnold for all his useful ideas and Laurens Smulders for many a statistical eye-opener. ML is supported by an ESA external fellowship. This research has made use of the Simbad database, operated at CDS, Strasbourg, France. All FFT computing in the reduction proces was done on the Cray−C98 of the National Facility for Supercomputing in Amsterdam.

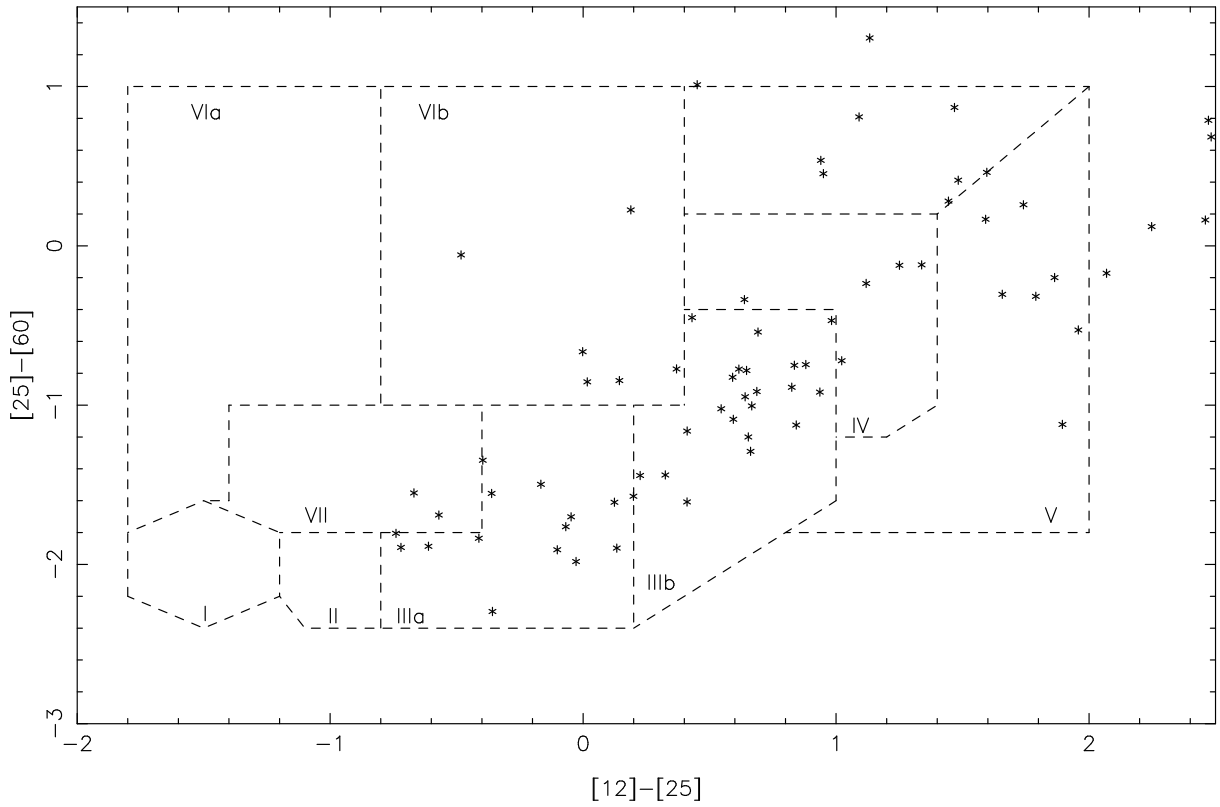

Fig. 7. The IRAS two-colour diagram for sources with an IRAS identification lying within the IRAS error ellipse (Col. 17 $\leq$ 1) with well-determined IRAS 12,25 and 60 μm flux densities (i.e. no upper limits). The regions marked IIIa and IIIb roughly outline the regions where classical OH/IR stars are expected (van der Veen & Habing 1988). The colours are defined as $[12]-[25] = 2.5\ ^{10}\log(S_{25}\ /\ S_{12})$. Features in this diagram will be discussed in future articles

Appendix A: Reduction method

A.1. Considerations

The reduction of the acquired data calls for a special strategy for a number of reasons. What we describe here is the process of searching the data for sources after the calibration described in Sect. 3.

In creating this strategy the following facts have to be dealt with:

a) The size of the dataset of 539 fields consisting of 512 spectral channels and a spatial extent of $42'\times 42'$ with a FWHM of the synthesized beam of $6''$ is of the order of a few hundred GBytes when fully imaged.
b) The synthesized beam pattern resulting from taking several short cuts spread over 12 h with a one-dimensional array has almost point-like sidelobes. The strength of the first sidelobe can be ∼50%. For strong sources, the sidelobes can be higher than the detection level up to 3° away from the real position. These sidelobes do not only create the possibility of obtaining wrong positions for sources, but also mask out fainter sources that by chance are in the same velocity channel. (See for instance spectrum #109 with sidelobes of #98).
c) Even after the editing mentioned in Sect. 3, radio-frequency interference (RFI) has an effect on images that is not easy to predict. It confuses standard astronomical data processing routines because it does not satisfy the general assumption of stationary sources.

Corresponding requirements were made for a possible reduction strategy:

a) It has to be highly automated, fast and efficient in its use of disk space. We cannot make and store full spectral-line cubes nor inspect them by eye.
b) It has to deal with sidelobes of sources that are not in the current field. Simply correlating peaks with the synthesized beam pattern does not enable us to discriminate between primary and secondary peaks, because of the way the visibility plane is sampled and weighted.
c) It must be robust in its ability to discriminate between astronomical sources and RFI.

A.2. Assumptions

There are three major assumptions we make to justify our strategy.

Firstly, we assume the sources we are looking for are point sources. Secondly, we assume the whole region of the survey is covered entirely within the width of the primary beam out to the offset where the primary-beam response in the main lobe equals the response of the first primary-beam sidelobe (see the mark "max" in Fig. 4a). It then follows that if we see the same spectrum (save a factor in flux density) at different positions in different fields, the brightest represents the real star. Thirdly, we assume the flux density of most of the stars we expect to find is too low for detection in a vector-averaged visibility spectrum with zero phase offset, so we do have to Fourier transform the visibility data and search in the image domain.

These three assumptions are all justified for the data we are presently discussing; there is only one exception to the first assumption in that source #153 (Table 1) is probably a nearby object and slightly resolved.

A.3. Method

The stategy developed is as follows:

1) MPFND

We Fourier transform one channel at a time, keeping it in memory. This image is then searched for its one highest peak value. If the shape of the peak is approximately Gaussian (i.e. a point source) and above a certain detection level, we write its velocity and fitted spatial position to an output file, otherwise we discard it. The image is then discarded. This process is repeated for all channels and for a number of neighbouring fields. Each field has a separate output file.

2) Model correlation

The output files of different fields are then individually searched for detections at the same position in a number of neighbouring channels. These detections are then marked as "models". If there are models in two (or more) different fields at the same velocity within a certain distance of each other, the brightest is assigned real and the others (assumed to be sidelobes) are shifted in position to the real position.

3) UVSUB

The consolidated point source models for each field are subtracted from the visibility data and the process starts again at step (1), now with a lower detection level and the new visibility data.

The whole cycle from step (1) to (3) is called a "pass". This way we build the stellar spectra in subsequent levels and find fainter sources in channels where bright sources were found in the first passes.

A.4. Implementation

1) MPFND

The main routine of the method is MPFND which does the imaging and the searching. It is a derivative of the existing MIRIAD imaging routine INVERT (version 18 Nov. 94). This is the most time-consuming part of the reduction and this routine as well as UVSUB and UVLIN was run on a Cray−C98. The less time-consuming part of correlating the model files was done on a local workstation since it requires more interaction and does not act directly on the visibility data.

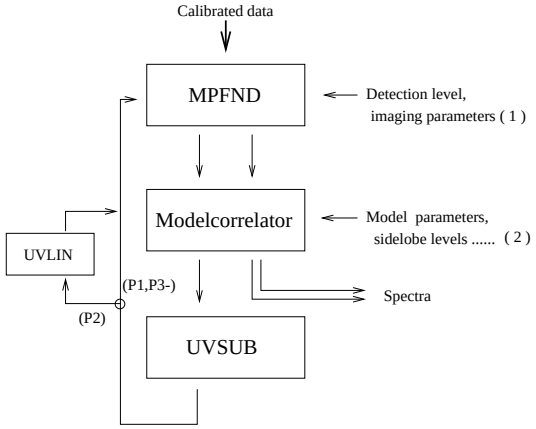

Fig. A1. Schematic representation of the reduction method. Every main cycle through MPFND, the model correlation and UVSUB is called one pass. At the end of the first pass (P2) UVLIN is applied. The input parameters at (1) and (2) can be adapted according to spectral features of the sources looked for and several features of the visibility data (see Sect. A4)

When imaging we used a natural weighting scheme of the visibilities, without any tapering, to get the maximum SNR. This does increase the sidelobe levels, but the method deals with that. The visibility data from the shortest baseline were always excluded from the imaging because of RFI.

The input at label (1) in Fig. A1 consists of the cell size, image size, detection level and the width of the boundary region of each image to exclude from the searching.

The detection levels in subsequent passes were decreased by $\sigma_{\rm theor}$ starting at $8\sigma_{\rm theor}$ ($\sigma_{\rm theor}$ is the noise level as theoretically calculated from the visibilities). In the last pass, for homogeneity, the detection level was fixed to 120 mJy for all fields. This level equals 3 to 4 $\sigma_{\rm emp}$ for 90% of the fields (see Sect. 5.1). The levels were chosen to ensure firstly that all sources bright enough to influence polynomial fitting (see Sect. A5) are subtracted in the first and second passes and secondly that the flux densities of the sources found in a pass are comparable to the detection level of that pass. It is important to find stars in as early a pass as possible, because at lower levels there are more and more noise detections and the process of correlation (see below) becomes more and more time-consuming. This is the reason for not making six passes all with a detection level of 120 mJy, which in principle would yield the same result.

To increase the speed of the transforms in the first two passes the images were made with a cell size of $5''\times\ 10''$. This causes some loss in SNR, but, since we only search for very bright sources in those passes, the SNR is still higher than 20. In the following passes cell sizes of $2''.5 \times 5''$ were used. [3] The size of the images was always $42'$ to ensure ample overlap between them. (This corresponds to an image size of 512×256 and 1024×512 cells respectively). The cell size was not optimized for all individual pointings but we chose to make the procedure as uniform as possible. To avoid the detection of Fourier transform errors, that are strongest at the boundaries of the images, the outer five cells were excluded from searching in the first two passes and in later passes the outer 10 cells, because at lower detection levels the imaging errors become relatively more important. After finding a peak in an image an area of 3×3 pixels around it was fitted with a two-dimensional parabola (see Sect. 5.2). If this fit indicates a position that is more than one cell size away from the peak pixel this indicates a highly non-Gaussian shape of the peak under consideration, since the peak of a Gaussian is roughly parabolic. This can be safely used as a criterion for interference or other unwanted detections and such peaks were discarded.

2) Model correlation

The inputs at (2) in Fig. A1 are relatively complicated to determine. In all passes, peaks at different velocities are identified as coming from the same source when positional coincidence is smaller than 0.35 cell size. This value was found empirically to be smaller than the typical difference in position between noise or interference peaks, correlated in neighbouring channels and bigger than the scatter expected in the positions of a source found in different channels (Sect. 5.2). Depending on the detection level and the strength of the highest peak found in the pass the distance out to which sidelobes can be expected has to be set. For the first pass this is as much as $3^{\circ}.0$ in declination[4]. After subtracting the brightest sources the distance quickly decreases to about $0^{\circ}.5$, so that sidelobes are found only in directly neighbouring fields. All 539 fields of the Bulge region were processed through each pass simultaneously, so that all models could be correlated optimally. Only detections in the outermost fields surrounding the whole region of 539 fields had to be checked for sidelobes from unobserved regions, since there the sidelobe detection assumption of complete coverage broke down. This was done by verifying the presence of a point source pattern by eye in the image plane at the detected channels.

Neighbouring channels are correlated by 16% after Hanning smoothing, which is enough to smear out a large number of noise peaks over two channels. Therefore, we required that detections be present at the same position in at least three channels (either directly neighbouring or within a velocity range reasonably expected from outflow velocities) for a detection to be trusted. At lower detection levels statistical considerations put a lower limit on the number of channels for a detection. There can be "false detections", that is a number of detections at the same position that meet the requirements mentioned above but are purely a statistical coincidence. At the 5σ level the expectation value of the total number of false detections in the whole data set is far less than one when the signal is demanded to be detected in three neighbouring channels at the same position. For the 4σ level the expected number is close to one. If we allow the third detected channel to be within a velocity range of $\pm$ 100 $\mathrm{km\,s^{-1}}$ from the other two neighbouring channels, the expected number is as much as one hundred. Such "false detections" could be identified as a double-peaked source. Therefore, at detection levels lower than 5σ, at least four detections, either in one peak over four neighbouring channels or in two separate peaks, are demanded at the same position. This gives an expected number of false detections of $\sim 10^{-3}$ for detection levels $\geq 4\sigma$ up to a few for the lowest detection level of 3σ.

3) UVSUB

The flux densities of all the point source models were determined with UVFLUX from the actual data at the velocities and the fitted (and for sidelobes shifted) positions found in the model correlation. They were then subtracted from the visibilities with UVSUB, via a direct Fourier transform.

A.5. Further implementations

To remove RFI from the visibilities, an 11^{th}-order polynomial fit (UVLIN, Sault 1994) to the real and imaginary parts of the visibilities was subtracted from the data between the second and third pass. By doing it at this stage, fitting bright OH sources was avoided, because all sources brighter than $\sim$1 Jy had been subtracted. Fitting spectra of brighter sources could cause serious problems over the whole spectral band and especially at the edges, because too much intensity would be put in the higher order terms of the polynomial.

It should be noted that it is possible for a source to be wrongly identified as a sidelobe of another star. This is not a problem, since the model that is subtracted from the visibility data is correct if the correct flux density level is

[3] In all passes the cell size roughly equals the HWHM of the synthesized beam, because when imaging with a cell size of $5''\times\ 10''$ those visibilities observed on long baselines will be discarded and the resulting synthesized beam will have larger HWHM. Therefore, the accuracy of the fitted position (Sect. 5.2, Fig. 5) is of the order of 0.2 cell sizes in all passes, and, since the SNR in the first passes is high, it is easily seen from Fig. 5 that the absolute value of this error should be roughly the same for all passes.

[4] The size synthesized beam of the ATCA in this region of the sky in the north-south direction (declination) is twice that in the east-west direction (right ascension). As a consequence, the synthesized-beam highest sidelobes are found twice as far away in declination as in right ascension, but with similar strength.

determined at the position of that other star. If a detection reoccurs after identifying it as a sidelobe and subtracting a corresponding point source model in the previous pass, then obviously the identification as a sidelobe was wrong and it should now be modelled as a real star. Therefore, we never subtracted the same model from the data twice.

Finally, we checked the spectra by eye, extracting them from the original data with UVSPEC (shown in Fig. A2). This is not necessary in principle with data that contain only sources and random noise. However, in our data, RFI introduces too much correlated signal that masquerades as sources. After the visual inspection, the limiting flux density, corrected for primary beam attenuation, is found to be 160 mJy (see Figs. 4b, f) or, in other words, $\sim 4\sigma$.

A.6. Discussion

Essentially, our method is a modification of the traditional method of CLEAN (Högbom 1974), in the sense that models are subtracted from the data at successive flux density levels. It is, however, stripped of every performance that is superfluous for processing the present data. Since in the present observations the sky does not feature bright extended emission and we want to find only point sources, in principle one cycle is sufficient to find the model. This model is then subtracted with loop gain 1 from the ungridded visibilities (similar to the Cotton-Schwab CLEAN algorithm, Schwab 1984). Therefore RFI and boundary imaging errors do not influence MPFND as much as they do standard implementations of CLEANing. MPFND is a fast method because it does not perform any convolution in the image plane, which is not necessary when one assumes that one iteration and loop gain 1 are best to find the models. Models are subtracted directly from the complex visibilities. Together with the fact that no disk I/O is needed to store cubes, this reduces the time needed for finding and subtracting models by a factor of four. In various fields we tested that the results of MPFND are exactly the same as those of other CLEAN methods with appropriate input values.

Table 1. Compact OH-maser sources in the galactic Bulge region.

The columns of Table 1 contain the following information:

1 Sequence number (coincident with spectra in Fig. A2).
2 Name in the OH$\ell - b$ convention.
3 Type indication
  * D = double-peaked spectrum
  * S = single-peaked spectrum
  * I = irregular spectrum.
4 Right ascension of the brightest peak for epoch J2000 (typical error $0\overset{''}{.}22$).
5 Declination of the brightest peak for epoch J2000 (typical error $0\overset{''}{.}44$).
6 Mean scatter of the position of the star in all channels where it was detected, in arcseconds on the sky (Eq. (1), Sect. 5.2).
7 Radial offset of the source from pointing centre.
8 Line-of-sight velocity with respect to the LSR of the blue-shifted (L) peak. For S and I spectra the velocity of the peak is always given as blue-shifted for reasons of tabulation (typical error 1 $\mathrm{km\,s^{-1}}$).
9 Same for the red-shifted (H) peak (typical error 1 $\mathrm{km\,s^{-1}}$).
10 Stellar velocity (typical error 1 $\mathrm{km\,s^{-1}}$).

$$v_\mathrm{c} = 0.5 \cdot (v_\mathrm{H} + v_\mathrm{L})\,. \tag{A.1}$$

11 Outflow velocity; zero for S and I sources (typical error 1 $\mathrm{km\,s^{-1}}$).

$$v_\mathrm{exp} = 0.5 \cdot (v_\mathrm{H} - v_\mathrm{L})\,. \tag{A.2}$$

12 Flux density, corrected for primary-beam attenuation, of the blue-shifted (L) peak (typical error 5%).
13 Same for the red-shifted (H) peak (typical error 5%).
14 Empirical noise in all empty planes for the present field (Fig. 3, Sect. 5.1).
15 Reference for previous OH maser detection (see Table 2 and Sect. 5.6).
16 Nearest IRAS PSC position (Sect. 5.5)
17 Ratio between the size of the error ellipse of the nearest IRAS point source and the distance to nearest IRAS PSC position in the direction of the OH position (Sect. 5.5).

(The table is available in electronic form via anonymous ftp (ftp 130.79.128.5) or through the World Wide Web at http://cdsweb.u-strasbg.fr/Abstract.html).

Table 2. References for previous OH maser detections (Table 1, Col. 15)

01 te Lintel Hekkert et al. 1991
02 te Lintel Hekkert et al. 1989
03 Becker et al. 1992
04 Lindqvist et al. 1992
05 Blommaert et al. 1994
06 Bowers & Knapp 1989
07 David et al. 1993
08 van Langevelde et al. 1992
09 Braz & Epchtein 1983.

Fig. A2. On the following pages the spectra for all the sources in Table 1 are shown. They are displayed with 50 $\mathrm{km\,s^{-1}}$ (except #008, #200 that have outflow velocities higher than 50 $\mathrm{km\,s^{-1}}$) on either side of the stellar velocity (if possible; for sources at the edge of the observed velocity range the unobserved part of the spectra is left blank, e.g. #179). The channel width used in the spectra is 1.46 $\mathrm{km\,s^{-1}}$ which is equal to the velocity resolution. Along the upper border of each spectrum the entry number of the source in Table 1 is given, along with its usual OH$\ell - b$ name, its identification as a D, S or I source (see Table 1, Col. 3) and the number of the reference in the case of previously known sources. The spectra are extracted from the original visibilities by the MIRIAD routine UVSPEC and the baselines are fitted with polynomial of order up to three. This means that interference still shows in the spectra. Also sidelobes from neighbouring stars are present in some spectra. If there is possible ambiguity in the interpretation of the spectra the detected peaks are marked with an

asterisk; other peaks in such spectra are not necessarily connected to the same source. The spectra were left relatively unprocessed in order to give a fair view of the data quality. (This figure is included in the electronic version of the paper, available at http://www.ed-phys.fr. The individual spectra are available upon request in more workable ascii-format (e-mail: sevenste@strw.leidenuniv.nl)).

References

Baud B., Habing H.J., Matthews H.E., O'Sullivan J.D., Winnberg A., 1975, Nat 258, 406

Becker R.H., White R.L., Proctor D.D., 1992, AJ 103, 544 (03)

Blommaert J.A.D.L., van Langevelde H.J., Habing H.J., van der Veen W.E.C.J., Epchtein N., 1992, in: Warner B. (ed.) Variable Stars and Galaxies, p. 269

Blommaert J.A.D.L., van Langevelde H.J., Michiels W.F.P., 1994, A&A 287, 479 (05)

Bowers P.F., Knapp G.R., 1989, ApJ 347, 325 (06)

Braz A., Epchtein N., 1983, A&AS 54, 167 (09)

Chapman J.M., Cohen R.J., 1986, MNRAS 220, 513

Cohen R.J., 1989, Rep. Prog. Phys. 52, 881

David P., Le Squeren A.M., Sivagnanam P., 1993, A&A 277, 453 (07)

Eder J., Lewis B.M., Terzian Y., 1988, ApJS 66, 183

Elitzur M., Goldreich P., Scoville N., 1976, ApJ 205, 384

Habing H.J., 1993, in: Dejonghe H., Habing H.J. (eds.) Proc. IAU Symp. 153, Galactic Bulges. Reidel, Dordrecht, p. 57

Habing H.J., 1996, ARA&A 7, 97

Högbom J., 1974, A&AS 15, 417

Lindqvist M., Winnberg A., Habing H.J., Matthews H.E., 1992, A&AS 92, 43 (04)

Kwok S., 1993, ARA&A 31, 63

Olofsson H., 1994, in: Jorgensen U.G. (ed.) Proc. IAU Coll. 146, Molecular Opacities in the Stellar Environment. Springer-Verlag, p. 113

Renzini, 1981, in: Iben, Renzini (eds.) Physical Processes in Red Giants, p. 431

Reynolds J., 1994, AT Tech. Doc. Ser. 39.3, 040

Sault R.J., 1994, A&AS 107, 55

Sault R.J., Teuben P.J., Wright M.C.H. , 1995, in: Shaw R.A., Payne H.E., Hayes J.J.E. (eds.) PASPC 77, Astronomical Data Analysis Software and Systems IV, p. 433

Schwab F.R., 1984, AJ 89, 1076

te Lintel Hekkert P., Versteege-Hansel H.A., Habing H.J., Wiertz M., 1989, A&AS 78, 399 (02)

te Lintel Hekkert P., Caswell J.L., Habing H.J., Haynes R.F., Norris R.P., 1991, A&AS 90, 327 (PTL) (01)

te Lintel Hekkert P., Chapman J.M., Zijlstra A.A., 1992, ApJ 390, L23

van Langevelde H.J., Frail D.A., Cordes J.M., Diamond P.J., 1992, ApJ 396, 686 (08)

van der Veen W.E.C.J., Habing H.J., 1988, A&A 194, 125

Vassiliadis E., Wood P.R., 1993, ApJ 413, 641

Whitelock P.A., Feast M., 1993, in: Weinberger R., Acker A. (eds.) Proc. IAU Symp. 155, Planetary Nebulae. Reidel, Dordrecht, p. 251

Wieringa M., Kesteven M., 1992, AT Tech. Doc. Ser. 39.3, 024

Wilson W.J., Barett A.H., 1968, Sci 161, 778

Zijlstra A.A., te Lintel Hekkert P., Pottasch S.R., et al., 1989, A&A 217, 157